

1 **Title: Cyto-architecture constrains a photoactivation induced tubulin gradient in**
2 **the syncytial *Drosophila* embryo**

3
4

5 Sameer Thukral¹, Bivash Kaity^{2*}, Bipasha Dey^{1*}, Swati Sharma¹, Amitabha Nandi²,
6 Mithun K. Mitra² and Richa Rikhy^{1#}

7
8 * equal contribution

9
10 **Affiliation and contact information**

11 1, Biology, Indian Institute of Science Education and Research, Homi Bhabha Road,
12 Pashan, Pune, 411008, India Phone: +91-20-25908065

13 2, Department of Physics, Indian Institute of Technology, Mumbai, 400076, India

14
15 #To whom correspondence is addressed: richa@iiserpune.ac.in

16
17 **Key words:** syncytium, photoactivation, *Drosophila*, embryogenesis, morphogen

18 gradient, Bicoid
19

20 **Running Title:** Gradient shape in syncytial *Drosophila* embryo

21
22 **Abbreviations:** Photoactivation (PA), Rho-GTP exchange factor 2 (RhoGEF2)

23
24 **Abstract**

25 *Drosophila* embryogenesis begins with nuclear division in a common cytoplasm forming
26 a syncytial cell. Morphogen gradient molecules spread across nucleo-cytoplasmic
27 domains to pattern the body axis of the syncytial embryo. The diffusion of molecules
28 across the syncytial nucleo-cytoplasmic domains is potentially constrained by
29 association with the components of cellular architecture, however the extent of
30 restriction has not been examined so far. Here we use photoactivation (PA) to generate
31 a source of cytoplasmic or cytoskeletal molecules in order to monitor the kinetics of their

32 spread in the syncytial *Drosophila* embryo. Photoactivated PA-GFP and PA-GFP-
33 Tubulin within a fixed anterior area diffused along the antero-posterior axis. These
34 molecules were enriched in cortical cytoplasm above the yolk-filled center suggesting
35 that the cortical cytoplasm is phase separated from the yolk-filled center. The length
36 scales of diffusion were extracted using exponential fits under steady state
37 assumptions. PA-GFP spread to greater distance as compared to PA-GFP-Tubulin.
38 Both gradients were steeper and more restricted when generated in the center of the
39 embryo probably due to a higher density of nucleo-cytoplasmic domains. The length
40 scale of diffusion for PA-GFP-Tubulin gradient increased in mutant embryos containing
41 short plasma membrane furrows and disrupted tubulin cytoskeleton. The PA-GFP
42 gradient shape was unaffected by cyto-architecture perturbation. Taken together, these
43 data show that PA-GFP-Tubulin gradient is largely restricted by its incorporation in the
44 microtubule network and intact plasma membrane furrows. This photoactivation based
45 analysis of protein spread across allows for interpretation of the dependence of gradient
46 formation on the syncytial cyto-architecture.

47

48 **Introduction**

49 Insect embryos initiate their development in a large syncytial cell where multiple nuclei
50 undergo nuclear divisions in a common cytoplasm without forming complete cells. The
51 cytoplasm is thought to mix uniformly in the syncytial cells. However, syncytial
52 *Drosophila* embryos have distinct domains of gene expression patterns in nuclei despite
53 being in this common cytoplasm (Shvartsman *et al.*, 2008). Several tissues in different
54 organisms, for example, plant endosperm cells, animal muscle cells and fungal hyphae,
55 also contain syncytial cells. Syncytial nuclei in fungi maintain distinct cell cycle stages
56 (Anderson *et al.*, 2013; Dundon *et al.*, 2016). The spatially separated daughter nuclei in
57 these fungi continue to proceed through the cell cycle synchronously by maintaining a
58 similar concentration of cell cycle components (Lee *et al.*, 2013). Syncytial nuclei in
59 muscle cells have a differential expression of mRNAs as compared to their neighbors
60 (Pavlath *et al.*, 1989). These studies indicate that several components of the cytoplasm
61 have local function and are likely to be generated and sequestered in the vicinity of the

62 syncytial nuclei. It is of interest to understand the cellular mechanisms that regulate
63 compartmentalized distribution of molecules despite being in a common cytoplasm.

64

65 The syncytial embryos of *Drosophila* provide a tractable system to decipher the extent
66 to which different cellular components are shared across nucleo-cytoplasmic domains.
67 *Drosophila* embryogenesis begins with 9 nuclear division cycles deep within the embryo
68 during the preblastoderm stage. Nuclei along with centrosomes migrate to the cortex in
69 nuclear cycle 10 and the nuclear division cycles 11-14 occur beneath the cortex in the
70 syncytial blastoderm embryo (Foe and Alberts, 1983; Karr, 1986; Warn, 1986; Foe, Odell
71 and Edgar, 1993; Sullivan and Theurkauf, 1995). Each interphase nucleus of the
72 syncytial blastoderm embryo is surrounded by apical centrosomes and a microtubule
73 array in an inverted basket conformation. Astral microtubules reach out from the
74 centrosomes towards the cortex and overlap with the astral microtubules originating
75 from neighbouring nuclei (Cao *et al.*, 2010). F-actin is present in caps above the nuclei
76 and centrosomes. Lipid droplets and yolk are enriched at the bottom of the basket
77 (Kuhn *et al.*, 2015; Mavrakis *et al.*, 2009a; Schmidt and Grosshans, 2018; Welte, 2015).
78 Each nucleo-cytoplasmic domain in the blastoderm embryo is associated with
79 organelles such as the endoplasmic reticulum, Golgi complex and mitochondria
80 (Frescas *et al.*, 2006; Mavrakis *et al.*, 2009b, Chowdhary *et al.*, 2017). The microtubule
81 and the actin cytoskeleton remodel during prophase and metaphase of the syncytial
82 division cycle. The centrosomes move laterally during prophase and give rise to
83 spindles during metaphase. Actin is enriched along the cortex at the extending plasma
84 membrane furrows (Foe, Odell and Edgar, 1993). The short furrows present in
85 interphase between adjacent nuclei extend deeper between spindles in metaphase.
86 Molecules in the plasma membrane, ER, Golgi complex and mitochondria have limited
87 exchange between adjacent nucleo-cytoplasmic domains in the syncytial *Drosophila*
88 embryo (Frescas *et al.*, 2006; Mavrakis *et al.*, 2009b, Chowdhary *et al.*, 2017).

89

90 Analysis of exchange of molecules in the cytoplasm or cytoskeleton across the syncytial
91 nucleo-cytoplasmic domains remains to be documented in a systematic manner, though
92 several studies have probed various cytoplasmic properties. Fluorescent dextran of

93 various sizes when injected in the cytoplasm of the syncytial blastoderm embryo has
94 been used to estimate the rate of cytoplasmic diffusion in the embryo (Gregor *et al.*,
95 2005). Micro-rheology based measurements of cytoplasmic viscosity have found that
96 cytoplasmic viscosity is three times higher than that of water in the region between nuclei
97 and yolk of the syncytial *Drosophila* embryo. In addition, microtubules, but not actin
98 contribute to the observed viscosity (Wessel *et al.*, 2015).

99

100 Morphogen gradient formation in the syncytial *Drosophila* can be used as a paradigm to
101 estimate properties of the embryo cytoplasm. Bicoid forms a gradient in the antero-
102 posterior axis, patterning the head of the embryo (Gregor *et al.*, 2007). The Bicoid
103 gradient is present primarily in the cortical region of the embryo (Cai *et al.*, 2017). The
104 dorso-ventral gradient formed by Dorsal is compartmentalized to each nucleo-
105 cytoplasmic domain (DeLotto *et al.*, 2007) and modelling studies show that plasma
106 membrane furrows could restrict Dorsal gradient spread (Daniels *et al.*, 2012). The
107 Dorsal gradient formation on the ventral side depends on specific binding partners on
108 the ventral side (Carrell *et al.*, 2017). These studies together imply that the syncytial
109 blastoderm cortex shows gradients whose properties depend upon sequestration due to
110 interaction with other cytoplasmic components or the syncytial cyto-architecture.

111

112 In this study, we attempt to elucidate the extent of gradient spread across nucleo-
113 cytoplasmic domains of the syncytial *Drosophila* embryo using a comparison between
114 cytoplasmic PA-GFP and PA-GFP-Tubulin. Fluorescently labelled tubulin incorporates
115 well in the microtubule network and is also present in the cytoplasm. We use
116 photoactivation to generate a fixed population of PA-GFP or PA-GFP-Tubulin and find
117 that both diffuse in the cortical region as compared to the yolk filled central region of the
118 syncytial blastoderm embryo. The gradient of PA-GFP-Tubulin is more restricted as
119 compared to PA-GFP in the antero-posterior axis. PA-GFP and PA-GFP-Tubulin have a
120 decreased spread when generated in the middle of the embryo as compared to the
121 anterior. The PA-GFP-Tubulin gradient diffuses to a greater distance in mutants
122 showing a loss of plasma membrane furrows and disruption of the microtubule network.
123 The PA-GFP gradient is not affected in these mutants. Our study provides a framework

124 for assessing the regulation of gradient formation by its interaction with the syncytial
125 cytoarchitecture components and has implications on the spread of morphogen
126 gradients across different paradigms.

127

128 **Results**

129

130 **Cytoplasmic GFP and mCherry-Tubulin are enriched cortically in the syncytial** 131 **division cycles in the *Drosophila* embryo**

132 The syncytial *Drosophila* blastoderm embryo has a characteristic arrangement of
133 microtubules around each nucleus. Microtubules emanate from the apical centrioles and
134 spread vertically covering the nuclei in an inverted basket like arrangement (Karr, 1986;
135 Sullivan and Theurkauf, 1995). In order to test the extent of spread of molecules in the
136 cytoplasm we imaged embryos expressing GFP ubiquitously under the control of the
137 *ubiquitin* promoter. GFP is expected to be present primarily in the cytoplasm and is not
138 known to interact with any cytoplasmic components (Verkman, 1999). We compared the
139 expression of cytoplasmic GFP to fluorescently labelled tubulin as it would partition into
140 the cytoplasm and also incorporate into the microtubule cytoskeleton. For this we
141 imaged live embryos expressing fluorescently tagged alpha-Tubulin (UASp-mCherry-
142 Tubulin) (Rusan and Peifer, 2007) with *mat-Gal4-vp16* (*mat-Gal4*). We found that
143 cytoplasmic GFP was enriched cortically and accumulated inside the cortical nuclei
144 (Figure 1A). Accumulation of GFP occurs passively inside the nucleus as a result of its
145 small size which allows it to pass through the nuclear pore complex (Ruiwen Wang,
146 2007). The fluorescence intensity of cytoplasmic GFP progressively increased near the
147 cortex as syncytial division cycles progressed but remained above the yolk filled region
148 (Figure 1B, Movie S1). We noticed GFP fluorescence dropped to approximately 30%
149 between 32 to 36 μ m in syncytial cycle 14 (Figure 1E). mCherry-Tubulin was enriched
150 on apical centrioles, in microtubules spreading vertically from the cortex and in the
151 cytoplasm in the syncytial division cycles (Figure 1C, Movie S2). mCherry-Tubulin also
152 showed progressive accumulation of fluorescence signal near the cortex as the
153 syncytial cycles progressed (Figure 1D). mCherry-Tubulin fluorescence dropped to 30%
154 between 25 to 27 μ m beneath the cortex in syncytial cycle 14 (Figure 1F). Thus

155 cytoplasmic GFP and mCherry-Tubulin were concentrated near the cortex and further
156 enriched during the progression of the nuclear cycles. In addition, they were present in
157 a separate cortical layer of cytoplasm on top of and distinct from the inner yolk-filled
158 region of the embryo.

159

160 **Photoactivation generates a source of PA-GFP and PA-GFP-Tubulin at the**
161 **anterior that forms a cortical gradient along the antero-posterior axis**

162 Labelled tubulin had a cytoplasmic and a microtubule bound fraction, in contrast to
163 GFP, which had a cytoplasmic fraction in the *Drosophila* syncytial blastoderm embryo.
164 This gave us an opportunity to assess the diffusion of these two proteins in the
165 cytoplasm across nucleo-cytoplasmic domains. Computational simulations have
166 predicted that binding to microtubule network and movement on motors is sufficient for
167 partitioning the cytoplasm, in the absence of membrane boundaries in the syncytial
168 blastoderm embryo (Chen *et al.*, 2012). We therefore asked whether tubulin which
169 partitions partially into microtubules could be more restricted as compared to GFP in the
170 syncytial blastoderm embryo.

171

172 Photoactivation of cytoplasmic and cytoskeletal proteins has been used to generate a
173 local source of protein molecules for monitoring their directional spread in axons
174 (Gauthier-Kemper *et al.*, 2012; GuraSadovsky *et al.*, 2017). In order to differentially test
175 the spread of cytoplasmic and cytoskeletal proteins in the syncytial blastoderm embryo,
176 we used photoactivation to create a local source of fluorescent PA-GFP or PA-GFP-
177 Tubulin at different locations of the embryo (Figure 2A). Unlike morphogens such as
178 Dorsal and Bicoid, GFP and tubulin are not differentially distributed in the syncytial
179 embryo. PA-GFP and PA-GFP-alpha-Tubulin84B (PA-GFP-Tubulin) were expressed
180 individually in embryos by crossing the transgenic flies to *mat-Gal4*. A fixed area was
181 continuously photoactivated to form fluorescent PA-GFP/PA-GFP-Tubulin, thus creating
182 a local source of PA-GFP/PA-GFP-Tubulin at the anterior pole of the embryo (Figure
183 2B,D, Movie S3,4). The movies of PA-GFP photoactivation also showed the presence of
184 a strong autofluorescent signal at the base of the cortex comprising of yolk (Movie S3).
185 The movies of PA-GFP-Tubulin showed an increase in fluorescence in the cytoplasm

186 and PA-GFP-Tubulin was also incorporated in microtubules in interphase and in
187 metaphase spindles (Movie S4). Both PA-GFP and PA-GFP-Tubulin increased in
188 concentration by diffusion away from the source across the syncytial division cycles. A
189 kymograph obtained at the source of photoactivation showed a distinct increase in
190 amount of photoactivated molecules over time (Figure 2C,E). The kymograph also
191 showed that the fluorescent signal was enriched near the cortex and did not enter the
192 central yolk filled region of the embryo. An analysis of the directionality of spread
193 showed that both molecules spread to a greater distance cortically along the antero-
194 posterior axis (XY) as compared to the depth within the embryo (XZ) (Figure 2F,G). The
195 cytoplasm of syncytial *Drosophila* blastoderm embryo has a biphasic distribution with
196 cortical nucleo-cytoplasmic domains present above a barrier comprising of yolk and
197 other unknown components (Foe and Alberts, 1983; Wessel *et al.*, 2015). This
198 organization possibly allows for greater spread along the cortex in the antero-posterior
199 axis as compared to the centre.

200

201 **Anteriorly photoactivated PA-GFP and PA-GFP-Tubulin shows an exponential** 202 **gradient that is steeper for PA-GFP-Tubulin**

203 We next attempted to quantify the gradients obtained in the antero-posterior axis on
204 photoactivation of PA-GFP and PA-GFP-Tubulin anteriorly. We found that the
205 photoactivated probes spread further as the syncytial cycles progress (Figure 3A,B).
206 The fluorescence intensity of PA-GFP and PA-GFP-Tubulin increased with time at
207 different locations in the embryo (Figure 3C,D). The concentration of PA-GFP and PA-
208 GFP-Tubulin when measured at 11 μ m from the photoactivation source, increased with
209 time and reached saturation. The time taken to reach steady state increased as we
210 moved away from the photoactivation source. Temporal evolution of fluorescence at
211 x=38 μ m approached a steady state at later time points. In contrast, for x=165 μ m, the
212 concentration did not reach a steady value (Figure 3C,D). This is also apparent from the
213 temporal evolution of the rate of change of the concentration at these different locations
214 (Figure 3E,F). We used the steady state concentration profile and extracted the
215 characteristic length scales by fitting it to an exponential decay equation (Figure 3G,H).
216 PA-GFP and PA-GFP-Tubulin formed gradients of distinct length scales after activation

217 at the anterior pole (Figure 3I). We found that the length scale for PA-GFP ($186\pm 25\mu\text{m}$)
218 was significantly higher than PA-GFP-Tubulin ($70\pm 4\mu\text{m}$) (Figure 3J). The estimated
219 diffusion coefficient for PA-GFP was $44.25\mu\text{m}^2/\text{s}$ and PA-GFP-Tubulin was $20.87\mu\text{m}^2/\text{s}$
220 (refer to Materials and Methods). This is likely to be because PA-GFP-Tubulin, in
221 addition to being present in the cytoplasm is also engaged in forming the microtubule
222 cytoskeleton and this turnover makes it less available to diffuse as compared to PA-
223 GFP alone.

224

225 **Photoactivation of the cytoplasmic PA-GFP and PA-GFP-Tubulin in the middle of**
226 **the *Drosophila* embryo results in a gradient with a smaller length scale as**
227 **compared to the anterior activation**

228 The syncytial *Drosophila* embryo has three domains containing distinct patterns of
229 density of nuclei and packing (Blankenship and Wieschaus, 2001; Rupprecht *et al.*,
230 2017). The domains show different speeds of furrow extension during cellularization.
231 The anterior and posterior domain contain nuclei at a lower density as compared to the
232 middle domain and the cells formed have a shorter plasma membrane furrows as
233 compared to the middle domain in cellularization. This difference in architecture across
234 the antero-posterior axis is regulated by the patterning molecules Bicoid, Nanos and
235 Torso (Blankenship and Wieschaus, 2001). This difference in the density of nucleo-
236 cytoplasmic domains prompted a comparison of the extent of gradient spread, when it
237 originates in the middle of the embryo versus when it originates in the anterior domain
238 (Figure 2A).

239

240 We tested if there was a difference in kinetics of gradient formation when
241 photoactivation was carried out in the middle (Figure 4) of the embryo as compared to
242 the anterior (Figure 2,3). For this we photoactivated PA-GFP and PA-GFP-Tubulin
243 containing embryos in a fixed region in the middle of the embryo (Figure 2A, 4A,C).
244 Photoactivation produced a cortical gradient with a progressive increase in gradient
245 spread across the syncytial division cycles (Figure 4B,D-F, Movie S5,6). The gradient of
246 PA-GFP and PA-GFP-Tubulin spread to a greater extent in the antero-posterior axis

247 (XY) as compared to the depth of the embryo (XZ), away from the region of
248 photoactivation (Figure 4G,H).

249
250 Length scale values were extracted by fitting an exponential equation and it was found
251 that the extent of spread for both the probes was lower (PA-GFP $57.4 \pm 7 \mu\text{m}$, PA-GFP-
252 Tubulin $45.6 \pm 10 \mu\text{m}$) than that observed when photoactivation was performed anteriorly
253 (Figure 4I-K). We further analysed if there was any difference in the gradient formation
254 from the centre towards the anterior versus centre towards the posterior pole (Figure
255 4L,M). We found the length scales of the gradients did not differ in either direction
256 (Figure 4N). These analyses show that the gradient spreads uniformly across the
257 syncytial nucleo-cytoplasmic domains towards the anterior pole and the posterior pole
258 of the *Drosophila* embryo, negating the presence of any cytoplasmic flows or currents.
259 In summary, photoactivated molecules generated in middle spread to a smaller distance
260 as compared to when they were generated at the anterior pole.

261
262 **Anteriorly photoactivated PA-GFP-Tubulin gradient length scale increases in**
263 **embryos containing an overexpression of RhoGEF2 on loss of pseudocleavage**
264 **furrows**

265 The gradients produced by PA-GFP and PA-GFP-Tubulin provided a framework to test
266 the role of syncytial cytoarchitecture in regulating their diffusion. Each cortical nucleus in
267 the syncytial blastoderm embryo of *Drosophila* contains a small ingression of the
268 plasma membrane around it. Astral microtubules support ectopic furrows (Barmchi *et al.*,
269 2005; Cao *et al.*, 2008; Crest *et al.*, 2012). The plasma membrane furrows ingress
270 deeper in metaphase to form pseudocleavage furrows (Schmidt and Grosshans, 2018).
271 To test the role of furrows in regulation of gradient formation across the syncytial
272 nucleo-cytoplasmic domains, we performed photoactivation experiments in embryos
273 defective in furrow formation. RhoGEF2 is a Rho-GTP exchange factor specifically
274 needed for the formation of furrows in the syncytial embryo (Barmchi *et al.*, 2005; Cao
275 *et al.*, 2008; Crest *et al.*, 2012). Depletion of RhoGEF2 leads to shortened furrows and
276 increase in RhoGEF2 is likely to increase active Myosin II and abolish furrow formation
277 (Sherlekar and Rikhy, 2016; Zhang *et al.*, 2018). We overexpressed RhoGEF2 by

278 crossing flies containing *mat-Gal4* and UASp-RhoGEF2. Embryos overexpressing
279 RhoGEF2 showed short or missing furrows in metaphase (Figure 5A). The metaphase
280 spindles did not show a significant change in these embryos as compared to controls
281 (Figure 5A).

282
283 Next, we generated embryos expressing PA-GFP or PA-GFP-Tubulin along with
284 RhoGEF2 overexpression. We performed continuous photoactivation at the anterior
285 pole in a fixed area and followed the resultant gradient across time (Figure 5B,D, Movie
286 S7,8). We found that similar to the control embryos (Figure 2), the gradients evolved
287 over time (Figure 5B-G). Further, in spite of major contractions in the embryo yolk
288 (Movie S7,8), the activated fluorescent molecules remained near the cortex and did not
289 mix with the underlying inner yolk region of the embryo (Figure 5H,I). This was also
290 evident from the kymographs which showed undulations in the cortical layer of
291 fluorescence, yet maintaining a separation from the embryo's inner yolk region (Figure
292 5C,E). The PA-GFP gradients did not change in the embryos over-expressing
293 RhoGEF2 (Figure 5J). The PA-GFP-Tubulin gradient however changed significantly
294 (Figure 5K) when compared to their respective gradients in control embryos (Figure 2).
295 The length scales were extracted on fitting an exponential function to the concentration
296 profile obtained. It was found that PA-GFP-Tubulin ($161 \pm 30 \mu\text{m}$) gradient spread to a
297 greater extent in embryos overexpressing RhoGEF2 as compared to control embryos.
298 There was no significant difference in PA-GFP-Tubulin spread from PA-GFP
299 ($191 \pm 36 \mu\text{m}$) in RhoGEF2-OE embryos (Figure 5L). RhoGEF2 overexpression led to
300 loss of plasma membrane furrows and loss of restriction of PA-GFP-Tubulin gradient in
301 the syncytial *Drosophila* embryo.

302 303 **Anteriorly photoactivated PA-GFP-Tubulin gradient length scale increases in** 304 **mutants of EB1**

305 Microtubules emanate from the centrosome at the apical side and spread vertically
306 downwards in the syncytial blastoderm embryo (Kellogg *et al.*, 1988; Sullivan and
307 Theurkauf, 1995). EB1 is present at the growing end of microtubules and its depletion is
308 likely to disrupt the microtubule architecture (Rogers *et al.*, 2002). We depleted embryos

309 of EB1 by combining *eb1* RNAi to *mat-Gal4* to disrupt microtubule organization. The
310 microtubule staining was reduced in embryos expressing *eb1* RNAi expressing
311 embryos. Also the plasma membrane levels for Scribbled were lowered (Figure 6A).

312
313 We combined the *eb1* RNAi with flies expressing PA-GFP or PA-GFP-Tubulin and
314 performed anterior photoactivation experiments in a fixed area (Figure 6B,D, Movie
315 S9,10). We found that similar to the control embryos (Figure 2), the gradient evolved
316 over time (Figure 6B-G). Similar to RhoGEF2 overexpression embryos, in spite of major
317 contractions in the embryo yolk, the activated fluorescent molecules remained near the
318 cortex (Figure 6C,E) and did not mix with the underlying yolk region of the embryo
319 (Figure 6H,I). Length scales were extracted by fitting these gradients (Figure 6J,K) to an
320 exponential function. We saw that the PA-GFP gradient did not change, while PA-GFP-
321 Tubulin gradient in mutant embryos changed significantly. The length scale analysis
322 showed that PA-GFP-Tubulin ($96 \pm 9 \mu\text{m}$) in *eb1* RNAi spread more than control
323 embryos. There was no significant difference between the PA-GFP-Tubulin length scale
324 as compared to PA-GFP ($111 \pm 15 \mu\text{m}$) in *eb1* RNAi embryos, even though the PA-GFP
325 was more constrained than control embryos (Figure 6L). In summary, *eb1* mutant
326 embryos showed a disrupted microtubule architecture and showed a loss of restriction
327 of PA-GFP-Tubulin gradient in the syncytial *Drosophila* embryo.

328

329 Discussion

330 In this study, we have examined the distribution and diffusion of cytoplasmic
331 components of the *Drosophila* syncytial blastoderm embryo. We have used
332 photoactivation of cytoplasmic PA-GFP to analyze its distribution and diffusion across
333 nucleo-cytoplasmic domains of the syncytial *Drosophila* embryo and further compared it
334 to PA-GFP-Tubulin, which is present in the cytoplasm and is also incorporated in
335 microtubules. We find that the cytoplasmic components have an increased
336 concentration at the cortex near the nucleo-cytoplasmic domains. Photoactivation of
337 these components shows diffusion to a greater distance in the antero-posterior axis in
338 the cortex as compared to the depth of the embryo. Also photoactivated cytoplasmic
339 components diffuse less when generated at the center of the embryo as compared to

340 the anterior. Diffusion is constrained by interaction with the cyto-architecture
341 components of the syncytial blastoderm embryo (Figure 7).

342

343 ***Photoactivation as a method to study regional differences in kinetics of gradient*** 344 ***formation in the syncytial Drosophila embryo***

345 The use of photoactivatable GFP molecules allows for the creation of localized ectopic
346 gradients and enables us to follow their evolution in real time across the syncytial
347 nuclear cycles. Photoactivation has been used previously to analyze the spread of
348 morphogen gradients in similar contexts. Photoactivation of Dorsal-PA-GFP allowed an
349 analysis of the extent of its spread in the dorsal versus the ventral side of the syncytial
350 blastoderm embryo. Sequestration of Dorsal by signaling components and nuclear
351 capture on the ventral side gave a more constrained gradient as compared to the dorsal
352 side of the embryo (Carrell *et al.*, 2017). In our study we used two photoactivatable
353 proteins which are incorporated in all nucleo-cytoplasmic domains. This allows us to
354 quantify the differences in their diffusion due to inherent differences in their association
355 with cyto-architecture of the embryo. We found that PA-GFP and PA-GFP-Tubulin had
356 smaller length scales when activated at the center as compared to the anterior of the
357 syncytial blastoderm embryo. The restricted diffusion at the center of the embryo could
358 be a result of a difference in relative crowding of nucleo-cytoplasmic domains in these
359 two regions (Blankenship and Wieschaus, 2001; Rupprecht *et al.*, 2017). An increase in
360 the density of nucleocytoplasmic domains in the center could lead to greater
361 sequestration of cytoplasmic components in general, leading to a smaller length scale.
362 Alternatively this could also come about due to differences in protein degradation or
363 sequestration machinery between these two regions. Whether the difference in density
364 of nucleo-cytoplasmic domains also leads to change in viscosity in the two regions
365 remains to be examined.

366

367 ***Cytoplasm organization in cells***

368 The cytoplasm of majority of living cells can be described as an inhomogeneous, multi-
369 phasic medium. Images of different components when drawn to scale (Goodsell, 2013)
370 clearly convey the fact that the cytoplasm is quite contrary to the earlier picture of a

371 freely flowing medium. The cytoplasm can be likened to a complex medium comprising
372 of physical constraints and constraints due to binding and crowding. Fluorescent
373 dextran of various sizes when injected into cells partitions based on their size (Luby-
374 Phelps, 2000). This further corroborates the fact that the space available for various
375 cytoplasmic components is constrained depending on their size. The metabolic state
376 can also change properties of the cytoplasm in the bacterial cell into either a glass-like
377 or fluid-like state (Parry *et al.*, 2014). Cytoplasmic distribution can change depending on
378 the ability and strength of a cytoplasmic molecule to bind to other components. A
379 modelling based study showed that binding to negative end directed dynein motors on
380 the mitotic spindle was sufficient to partition the cytoplasm into two halves even without
381 the presence of any membrane bound compartments (Chen *et al.*, 2012).

382

383 Our finding that PA-GFP-Tubulin is more restricted in its spread as compared to PA-
384 GFP suggests that cytoplasmic components having multiple interactors are more
385 confined in their diffusion. For the syncytium, this property is beneficial, as components
386 produced from a syncytial nucleus tend to remain near their parent nucleus, with no
387 clear boundaries being present in the shared cytoplasm. This observation suggests that
388 different components in a cell could be restricted by distinct mechanisms, some binding
389 to microtubules, some to actin or some being sequestered in the nuclei or other
390 organelles ultimately resulting in restricting their action in space and time. The diffusion
391 of PA-GFP-Tubulin in our study increased on abrogation of the metaphase furrows and
392 microtubule cytoskeleton in embryos over-expressing RhoGEF2 and *eb1* RNAi, it
393 reached length scales similar to PA-GFP. This further suggested that binding and
394 sequestration were responsible for PA-GFP-Tubulin restriction. Loss of plasma
395 membrane furrows could also lead to disorganization of astral microtubules (Cao *et al.*,
396 2010; Crest *et al.*, 2012) in the periphery thereby increasing the effective diffusion of
397 PA-GFP-Tubulin.

398

399 Further, the observation that cytoplasmic components are cortically enriched
400 corroborates previously reported data about Bicoid movement in the cortex and its
401 dependence on the actin and the microtubule cytoskeleton of syncytial blastoderm

402 embryos (Cai *et al.*, 2017). SEM images from cross sectioned *Drosophila* embryos also
403 show the presence of similar biphasic compartments (Figard *et al.*, 2013; Turner and
404 Mahowald, 1976). Filamentous actin and non-muscle myosin are concentrated in the 3-
405 4 μ m and 1-2 μ m region of the “yolk-free” cytoplasm just beneath the plasma membrane
406 of the embryo, respectively (Foe, Odell and Edgar, 1993). The cortical yolk-free
407 cytoplasm increases in its depth as the syncytial cycles progress (Foe, Odell and Edgar,
408 1993). Our study is a further characterization of protein mobility in these phases, and we
409 show that the cortical cytoplasm and yolk beneath it seem to form two separate phases,
410 and do not mix in spite of major contractions of the embryo in mutant embryos. The size
411 of the cortical cytoplasmic region as determined by the spread of cytoplasmic GFP in
412 our study, is approximately 40 μ m, where the fluorescence intensity falls off sharply. This
413 observation raises further questions about how these two phases are separate and the
414 mechanisms that contribute to maintaining their integrity.

415

416 ***Implications on morphogen diffusion***

417 The observation about the presence of two separate phases of cortical cytoplasm and
418 embryo yolk provides an interesting perspective to our current understanding of the
419 morphogen gradients in the early embryo, namely, Bicoid, Dorsal and Torso. The Bicoid
420 gradient has been extensively studied using the framework of the synthesis, diffusion
421 and degradation (SDD) (Durrieu *et al.*, 2018; Gregor *et al.*, 2007; Grimm *et al.*, 2010)
422 and related models. However, a complete theoretical understanding of the mechanisms
423 underlying the formation of the Bicoid gradient is still lacking. Our finding implicates a
424 restriction of the effective volume in which Bicoid gradient develops and matures. It also
425 raises the possibility that various cytoarchitectural components could impinge on its
426 formation. For example, perturbations in furrows or cytoskeletal structures can change
427 the effective concentration of morphogens in the cortical cytoplasm, leading to changes
428 in the morphogen profiles, specifically for Bicoid.

429

430 There have also been various studies, implicating the size and shape of the mRNA
431 source in Bicoid gradient formation (Fahmy *et al.*, 2014; Little *et al.*, 2011; Spirov *et al.*,
432 2009). Photoactivation allows creation of different sized sources which can produce PA-

433 GFP/PA-GFP-Tubulin or morphogen gradients at different rates and provides an
434 opportunity to study the effect of the source on the gradient shape and dynamics.

435

436 The observation of distinct gradient length scales of PA-GFP-Tubulin versus PA-GFP
437 points to another facet of morphogen gradient formation, namely decrease in the
438 diffusivity of morphogens based on their interactions. FGF gradient is known to interact
439 with Heparan sulfate proteoglycans which changes the effective diffusivity of the
440 morphogen. The removal of these proteoglycans leads to an increase in the morphogen
441 spread (Balasubramanian and Zhang, 2016). We can interpret the difference between
442 the PA-GFP and PA-GFP-Tubulin profiles as being a consequence of increased binding
443 of tubulin to the microtubule architecture. This leads to increase in its residence time by
444 sequestration and thus a lower effective diffusion and consequently, a smaller length
445 scale. It would be interesting to analyse the effect of removal of binding interactions for
446 well-studied morphogen like Bicoid. It is notable that Dorsal gradient is known to be
447 modulated depending on the presence or absence of a dimerizing GFP (Carrell *et al.*,
448 2017).

449

450 Finally, our observation of difference in length scales between anterior versus centre
451 photoactivation suggests a difference in cyto-architectural properties for different
452 regions of the embryo. Our studies necessitate a systematic analysis of the impact of
453 local architectural properties in the formation and maintenance of morphogen gradients.

454

455 **Materials and methods**

456

457 ***Drosophila* stocks and crosses**

458 *Drosophila* stocks were maintained in standard corn meal agar at 25°C. All crosses
459 were set up at 25°C, except *eb1* RNAi (29°C). *mat-gal4-vp16*; *mat-gal4-vp16* (Girish
460 Ratnaparkhi, IISER, Pune, India) was used to drive mCherry-alpha-TubulinA1B
461 (mCherry-Tubulin) (#25774), PA-GFP (gift from Prof. Gerald M. Rubin, Janelia
462 Research Campus, VA, USA), PA-GFP-alpha-Tubulin84B (PA-GFP-Tubulin) (#32076),

463 UASp-RhoGEF2 (#9386) and *eb1* RNAi (#36599). GFP expressed under ubiquitin
464 promoter (*ubi*-GFP, #1681) was imaged directly.

465

466 **Microscopy**

467 1.5 hour old embryos were collected on sucrose agar plates, washed, dechorionated
468 using 100% bleach, mounted on coverglass chambers (LabTek, Germany) in PBS
469 (Mavrakis *et al.* 2008) and imaged on Plan-Apochromat 25x/0.8 Oil Immersion or Plan-
470 Neofluar 40x/1.30 Oil objective on Zeiss LSM780 or LSM710 systems. PA-GFP and PA-
471 GFP-Tubulin were photoactivated using the 405 nm diode laser using the bleach
472 module on the LSM software. PA-GFP and PA-GFP-Tubulin thus produced was imaged
473 using the 488 nm laser. ROI size was kept constant at 373 μ m². Photoactivation
474 iterations were kept constant at 10 iterations per frame with activation being performed
475 after every frame. The photoactivation was carried out for 0.36s (10 iterations). 512
476 pixel X 512 pixel images were acquired after that with a scan speed of 1.97 seconds per
477 frame. Mid sagittal sections were imaged. 8 bit images were acquired with mean line
478 averaging of 2. The gain and laser power were adjusted to be cover the dynamic range
479 of each fluorescent tag and care was taken to not reach 255 on the 8 bit scale. Pinhole
480 was kept open at 180 μ m.

481

482 **Immunostaining**

483 F1 flies were selected from Gal4 and mutant crosses were transferred to embryo
484 collection cages (Genesee Scientific, CA, USA) with 2.5% sucrose agar supplemented
485 with yeast paste. Embryos were washed, dechorionated using 100% bleach for 1 min,
486 washed and fixed in heptane: 4% paraformaldehyde (1:1) in PBS (1.8 mM
487 KH₂PO₄, 137 mM NaCl, 2.7 mM KCl, 10 mM Na₂HPO₄) for 20 mins at room temperature.
488 Embryos were devitellinized by vigorously shaking in heptane:methanol (1:1) for anti-
489 Tubulin and Scribbled immunostaining. 2% Bovine Serum Albumin (BSA) in PBS with
490 0.3% Triton X-100 (PBST) was used for blocking. Following primary antibodies were
491 diluted in the block solution: anti-Tubulin (Anti-mouse, Sigma-Aldrich, Bangalore,
492 India, 1:1000), anti-Scrib (Anti-Rabbit, Kind gift by Prof. Kenneth Prehoda, University of
493 Oregon, OR, USA, 1:1000). Fluorescently coupled secondary antibodies (Alexa Fluor

494 488, 568, 647 coupled anti-rabbit and anti-mouse, Molecular Probes, Bangalore, India)
495 were used at 1:1000 dilution in PBST. Embryos were imaged using LD LCI Plan-
496 Apochromat 25x/0.8 ImmKorr DIC M27 objective on the Zeiss LSM710/780.

497

498 **Image analysis**

499 Segmented lines of 10 or 20 pixel (10 or 20 μ m width) were drawn across the cortex
500 from the anterior to the posterior or centre to anterior/posterior of the embryo on the
501 dorsal and the ventral side. Line profile measurements, containing embryo length vs
502 intensity values were obtained using ImageJ. For XZ analysis, similar segmented lines
503 were drawn for a distance of 90 μ m from the place of activation, in XY or XZ directions.
504 The process was multiplexed using ImageJ macros. A MATLAB script was used to
505 process the generated files. The script rescales the embryo length from 0 to 1 in the
506 antero-posterior direction, subtracts the minimum intensity value, rescales it with the
507 maximum and smoothens the intensity values using sliding window averaging.

508

509 **Sampling and Statistics**

510 3 or more embryos as indicated in the corresponding figure legends were imaged and
511 quantified for each experiment. Graphpad Prism 5.0 was used for Statistical analysis
512 and plotting.

513

514 **Theory**

515 **Estimation of length scales from concentration profiles**

516 The time evolution of the concentrations of the photo-activated molecules were
517 analysed within the framework of the standard one-dimensional Synthesis-Diffusion-
518 Degradation (SDD) model in a domain of length L (Crick, 1970),

$$519 \quad \frac{\partial C(x, t)}{\partial t} = D \frac{\partial^2 C(x, t)}{\partial x^2} - \kappa C(x, t)$$

520 where, $C(x, t)$ represents the concentration of the photo-activated species as position x
521 at time t , D is the diffusion constant, and κ is the degradation rate. The mean lifetime of
522 the molecule τ is the inverse of the degradation rate, $\tau = 1/\kappa$. This equation is to be
523 solved subject to the appropriate boundary conditions, accounting for the presence of a
524 localised source of fluorescent molecules at the anterior pole of the embryo (or at the

525 centre in the case of centre activation), and reflecting boundary conditions at the
526 posterior pole,

$$527 \quad -D \frac{\partial C}{\partial x} \Big|_{x=0} = Q \quad \text{and} \quad D \frac{\partial C}{\partial x} \Big|_{x=L} = 0$$

528 and the appropriate initial condition reflecting the absence of any photoactivated
529 molecules for $t \leq 0$, $C(x, t \leq 0) = 0$.

530

531 At long enough times, the concentration profile evolves to a steady state (Figure 3C,D).

532 The steady state solution of the SDD model for a semi-infinite domain is given by,

$$533 \quad C_{ss}(x) = \frac{Q \lambda}{2 D} \exp(-x/\lambda)$$

534 where the characteristic length-scale lambda is defined as, $\lambda = \sqrt{D/\kappa} = \sqrt{D} \tau$. The semi-
535 infinite assumption holds if the characteristic length-scale is much smaller than the size
536 of the domain, $\lambda \ll L$.

537

538 If the length scale is comparable to the system size, then the steady state solution

539 depends on the length of the domain (size of embryo) and is given by,

$$540 \quad C_{ss}(x) = \frac{Q \lambda}{2 D} \left[\frac{e^{x/\lambda} + e^{(L-x)/\lambda}}{e^{L/\lambda} - 1} \right]$$

541

542 In order to ensure that the concentration profiles have reached a steady state, we plot
543 the concentration versus time plots and the rate of change of concentration for both PA-
544 GFP and PA-GFP-Tubulin. The time taken to reach the steady state depends on the
545 position along the AP axis, and is smaller for locations closer to the anterior pole. We
546 first show the results for PA-GFP-Tubulin (Figure 3F). As can be seen from the figures,
547 the tubulin concentration reaches a steady state fairly quickly, justifying the assumption
548 of the steady state for fitting the concentration profile. The time taken to reach the
549 steady state can be determined by the time at which the derivative dC/dt approaches
550 zero.

551

552 A similar analysis can be performed for PA-GFP (Figure 3E). The situation in this case
553 is more complex, with the locations closer to the anterior pole having reached a steady
554 state, while locations further away still evolving at the final time point of the experiments.

555 The larger time taken to reach the steady state for PA-GFP can be understood from the
556 fact that the length-scale for PA-GFP is much larger than PA-GFP-Tubulin and hence it
557 takes a correspondingly larger time for the concentration profile as a whole to reach
558 steady state. In this case, since the locations closer to the anterior pole have reached a
559 steady state, we can fit the concentration profile in a localised region closer to the
560 anterior pole.

561
562 The concentration profiles at the last time point are fitted by this steady state formula to
563 obtain the characteristic length-scale λ . The fits are shown for PA-GFP (Figure 3G) and
564 PA-GF-Tubulin (Figure 3H). This yields,

$$565 \lambda_{GFP} = 145 \pm 24.6 \mu m \quad \text{and} \quad \lambda_{tub} = 86 \pm 11.28 \mu m$$

566 The PA-GFP spreads to a much larger distance from the anterior pole than Tubulin-PA-
567 GFP.

568

569 **Estimation of diffusion constant from concentration profiles**

570 For the SDD model, the time taken to reach the steady state can be estimated
571 theoretically (Berezkhovskii *et al.*, 2010), and is given by ,

$$572 \tau_{ss}(x) = \frac{\tau}{2} \left(1 + \frac{x}{\lambda}\right)$$

573 Where, $\tau_{ss}(x)$ is the time taken to reach steady state at location x , and the mean lifetime
574 of the molecule is denoted by τ , as before. The above formula also supports the notion
575 that locations further away from the source at the anterior pole, take longer time to
576 reach steady state. For distances much smaller than the characteristic length-scale,
577 $x \ll \lambda$, the above equation reduces to $\tau_{ss}(x) = \tau/2$, and hence the mean lifetime can
578 be read off from the concentration plots (Figure 3C,D) and its derivative plots (Figure
579 3E,F) by noting the time taken to reach steady state for both PA-GFP and PA-GFP-
580 Tubulin for $x = 11 \mu m (x \ll \lambda)$. This yields,

$$581 \tau_{GFP} \approx 600 s \quad \text{and} \quad \tau_{tub} \approx 200 s$$

582 Combining the estimates of the length scale λ and the lifetime τ , we can then
583 independently obtain an estimate of the diffusion constant,

$$584 D = \lambda^2 / \tau$$

585 This gives,

586 $D_{GFP} \approx 44.25 \mu m^2/s$ and $D_{tub} \approx 20.87 \mu m^2/s$

587

588 The estimation of the time taken to reach steady state makes certain assumptions.
589 Firstly, the fluctuations in the concentration can be significantly high in certain embryos,
590 which results in a large variation of the time estimate. Secondly, a characteristic feature
591 of the time evolution of concentration profiles is that there is a sharp initial increase
592 followed by a slow increase in the concentration. This suggests that there may be other
593 biological processes beyond those described by the SDD model that affect the evolution
594 of the concentration to the steady state. While estimating the diffusion coefficient, we
595 neglect the slower variation and have chosen the onset of this slow increase as the
596 steady state time.

597

598 **Acknowledgements**

599 Stocks obtained from the Bloomington *Drosophila* Stock Center (NIH P40OD018537) were
600 used in this study. ST, BD, SS thank CSIR India for funding their fellowship. RR thanks
601 DBT, DST and IISER Pune for funding the lab. BK thanks MHRD for fellowship. MM thanks
602 DST Ramanujan Fellowship (13DST052) and IRCC, IIT Bombay for funding. AN
603 acknowledges IRCC, IIT Bombay, India, and SERB, DST, India (Project No.
604 ECR/2016/001967) for financial support.

605

606 **Figure Legends**

607 **Figure 1: Cytoplasmic GFP and mCherry-Tubulin are enriched cortically in the** 608 **syncytial division cycles**

609 A-D: Characterization of cortical spread of GFP and mCherry-Tubulin in the syncytial
610 division cycles. Images are shown from different cycles (NC11,12,13,14) of embryos
611 ubiquitously expressing GFP (A) or maternally expressing mCherry-Tubulin (similar
612 trends were observed for n=3 movies) (C). Kymographs show cortical enrichment of
613 fluorescent signal for GFP (B) and mCherry-Tubulin (D) over time. Scale bar=5 μ m,
614 600s.

615 E-F: Quantification of cortical enrichment of fluorescent signal in cytoplasmic GFP and
616 mCherry-Tubulin. Graph shows normalized intensity profile for GFP (E) and mCherry-
617 Tubulin (F) obtained from a line drawn from the cortical region towards the centre of the

618 embryo. The dashed line shows a point at which the intensity drops to 30%. Note that
619 the signal remains above the region containing the dark yolk filled vesicles.
620 The images are shown in a 16 color intensity rainbow where Blue represents the lowest
621 intensity and red represents the highest intensity. Scale bar= 10 μ m

622

623 **Figure 2: Anteriorly photoactivated PA-GFP and PA-GFP-Tubulin produces a**
624 **cortical gradient**

625 A. The photoactivation method to create an ectopic source of PA-GFP and PA-GFP-
626 Tubulin. Photoactivation was carried out in a fixed area (373 μ m²) in the anterior or the
627 center of the syncytial embryo. A kymograph monitoring the increase in signal was
628 drawn at the source (green bar). A cortical region was drawn to estimate the change in
629 intensity in the antero-posterior axis (orange). The exponential function was fit to
630 estimate the length scale of spread for the gradients.

631 B-E. Anteriorly photoactivated PA-GFP and PA-GFP-Tubulin forms a gradient. Images
632 for NC11,12,13,14 of embryos from expressing PA-GFP (B) or PA-GFP-Tubulin (D) are
633 shown after photoactivation at the anterior pole. Kymograph shows increase in cortical
634 fluorescence over time in PA-GFP (C) and PA-GFP-Tubulin (E) expressing embryo.
635 Scale bar=50 μ m,60s.

636 F-G. PA-GFP and PA-GFP-Tubulin spreads preferentially at the cortex. Graph
637 quantifying the extent of spread of photoactivated protein fluorescence in the planar or
638 antero-posterior XY axis vs depth or XZ direction for PA-GFP (F) and PA-GFP-Tubulin
639 (G) with a line drawn across either XY or XZ direction from the activated region. The
640 raw data is in a lighter color and the averaged data is in a darker color, error bars
641 represent standard error on means (n=3 embryos for PA-GFP-Tubulin and PA-GFP
642 each).

643 The images are shown in a 16 color intensity rainbow where Blue represents the lowest
644 intensity and red represents the highest intensity. Scale bar= 50 μ m.

645

646 **Figure 3: Anteriorly photoactivated PA-GFP and PA-GFP-Tubulin forms an**
647 **exponential gradient with PA-GFP-Tubulin being more restricted as compared to**
648 **PA-GFP**

649 A-B. Quantification of the photoactivated signal across nuclear cycles. Graph shows
650 intensity for PA-GFP (A) and PA-GFP-Tubulin (B) for one embryo with a line drawn
651 across the cortical region in the syncytial nuclear cycles. Similar profiles were observed
652 in multiple embryos (n=3 for each).

653 C-D. PA-GFP and PA-GFP-Tubulin increases in concentration over time. The graph
654 depicts increase in PA-GFP (C) or PA-GFP-Tubulin fluorescence intensity over time as
655 measured at different locations (11, 38, 165 μ m from the source of photoactivation at the
656 anterior).

657 E-F. Graph shows the rate of change in concentration of photoactivated PA-GFP (E)
658 and PA-GFP-Tubulin (F) to assess if the steady state has reached. Each plot is a
659 derivative of the corresponding plot in C,D.

660 G-H. Anteriorly photoactivated PA-GFP and PA-GFP-Tubulin shows an exponential
661 gradient. Raw experimental values (red) were fit to an exponential function (blue) for
662 each probe.

663 I. Quantification of intensity profile of photoactivated probe measured at the end of the
664 experiment for PA-GFP and PA-GFP-Tubulin. Graph shows raw data in a lighter color
665 and averaged data in a darker color, error bars represent standard error on means (n=3
666 embryos each for PA-GFP and PA-GFP-Tubulin).

667 J. Scatter plot of length scales extracted after fitting an exponential decay function to the
668 intensity profiles seen in I (n=6 regions drawn in 3 embryos for PA-GFP, 8,4 for PA-
669 GFP-Tubulin, Two tailed Mann-Whitney non-parametric test with p value=0.0007).

670

671 **Figure 4: Photoactivation of the cytoplasmic PA-GFP and PA-GFP-Tubulin in the**
672 **middle of the *Drosophila* embryo**

673 A-D. Monitoring gradient of center photoactivated PA-GFP and PA-GFP-Tubulin.
674 Images from NC11,12,13,14 expressing PA-GFP (A) or PA-GFP-Tubulin (C) and
675 photoactivated at the centre of the embryo are shown. Kymograph shows increase in
676 cortical fluorescence with time for PA-GFP (B) and PA-GFP-Tubulin (D) embryo. Scale
677 bar=50 μ m, 60s.

678 E-F. Quantification of evolution of photoactivated signal in syncytial nuclear cycles. The
679 graph depicts the fluorescence intensity for PA-GFP (E) and PA-GFP-Tubulin (F) from

680 one embryo for a line drawn from the source along the antero-posterior axis. Similar
681 profiles were observed in multiple embryos (n=3 for each).

682 G-H. Quantification of photoactivated protein in XY vs XZ direction for PA-GFP (G) and
683 PA-GFP-Tubulin (H). Graph shows intensity profile of a line drawn in the XY or XZ
684 direction from the activated region. The raw data is shown in a lighter color and the
685 averaged data is shown in a darker color, error bars represent standard error on means
686 (n=3 embryos for PA-GFP-Tubulin and PA-GFP each).

687 I-J. Graphs comparing the intensity profile obtained upon photoactivation at the anterior
688 pole versus the centre of the embryo for PA-GFP (I) and PA-GFP-Tubulin (J) (n=3
689 embryos for PA-GFP and PA-GFP-Tubulin each).

690 K. Scatter plot of the length scales extracted after fitting an exponential decay function
691 to the intensity profiles seen in I,J. The values of length scales for PA-GFP and PA-
692 GFP-Tubulin for anterior photoactivation are repeated from Figure 3J. (n=8,4 for PA-
693 GFP center activation, 6,3 for PA-GFP activated anteriorly, 6,3 for PA-GFP-Tubulin
694 center activation and 8,4 for PA-GFP-Tubulin anterior activation. Two tailed Mann-
695 Whitney non-parametric test with p value=0.0007 for PA-GFP and 0.04 for PA-GFP-
696 Tubulin).

697 L-M. Graphs comparing the intensity profiles obtained upon photoactivation at the
698 centre of the embryo for analysis of directionality of spread. Fluorescence intensity is
699 obtained from a line drawn from the centre activated region towards anterior or posterior
700 pole for PA-GFP (L) and PA-GFP-Tubulin (M). The raw data is shown in a lighter color
701 and the averaged data is shown in a darker color, error bars represent standard error on
702 means (n=3 embryos for PA-GFP-Tubulin and PA-GFP each).

703 N. Scatter plot of the length scales extracted after fitting an exponential decay function
704 to the intensity profiles seen in L,M. (n=4,4 for PA-GFP center activation, center to
705 anterior subset from K, 4,4 for PA-GFP center activation, centre to posterior subset from
706 K, 3,3 for PA-GFP-Tubulin center activation, centre to anterior subset from K and 3,3 for
707 PA-GFP-Tubulin center activation, centre to posterior subset from K. Two tailed Mann-
708 Whitney non-parametric test with p value=0.34 for PA-GFP and 1 for PA-GFP-Tubulin).

709 The images are shown in a 16 color intensity rainbow where Blue represents the lowest
710 intensity and red represents the highest intensity. Scale bar= 50µm.

711

712 **Figure 5: PA-GFP-Tubulin spreads to a greater extent in embryos containing**
713 **RhoGEF2 overexpression**

714 A. Embryos overexpressing RhoGEF2 show loss of metaphase furrows: Surface and
715 sagittal views of fixed control or RhoGEF2 overexpressing embryos, stained with
716 Tubulin (Red), Scribbled (Green) and DNA (Grey), show loss of furrows and no
717 significant effect on metaphase spindles (100%, n=30 embryos). Scale bar=10 μ m.

718 B-E. Images from syncytial cycles of an embryo co-expressing RhoGEF2 along with
719 PA-GFP (B) or PA-GFP-Tubulin (D) which has been photoactivated at the anterior pole.
720 Kymograph for PA-GFP (C) and PA-GFP-Tubulin (E) shows increase in cortical
721 fluorescence with time while sometimes changing the extent to which the fluorescence
722 is confined. Scale bar=50 μ m, 60s.

723 F-G. Quantification of evolution of the photoactivation across nuclear cycles in embryos
724 overexpressing RhoGEF2. A line profile was drawn in syncytial cycles is plotted for PA-
725 GFP (F) and PA-GFP-Tubulin (G) for one embryo. Similar profiles were observed in
726 multiple embryos (n=3 for each).

727 H-I. Quantification of extent of photoactivation in XY vs XZ direction for PA-GFP (H) and
728 PA-GFP-Tubulin (I) in embryos overexpressing RhoGEF2. The raw data is shown in a
729 lighter color and the averaged data is shown in a darker color, error bars represent
730 standard error on means (n=3 embryos for PA-GFP and PA-GFP-Tubulin each).

731 J-K. Quantification of intensity profile of photoactivated probe as measured at the end of
732 the experiment for PA-GFP (J) and PA-GFP-Tubulin (K) in embryos overexpressing
733 RhoGEF2. The raw data is shown in a lighter color and the averaged data is shown in a
734 darker color, error bars represent standard error on means (n=3 embryos for PA-GFP-
735 Tubulin and PA-GFP each). The graph for photoactivation of PA-GFP and PA-GFP-
736 Tubulin in control embryos is the same as that shown in Figure 3I and is repeated here
737 for comparison.

738 L. Scatter plot of the length scales extracted after fitting an exponential decay function
739 to the intensity profiles seen in J and K. The values of length scales for PA-GFP and
740 PA-GFP-Tubulin for anterior photoactivation in control embryos are repeated from
741 Figure 3J. (n=5,3 for PA-GFP in RhoGEF2-OE, 6,3 for PA-GFP-Tubulin in RhoGEF2-

742 OE. Two tailed Mann-Whitney non-parametric test, p value 0.53 for PA-GFP and PA-
743 GFP-Tubulin in RhoGEF2-OE, 0.93 for PA-GFP/RhoGEF2-OE and PA-GFP/control,
744 0.002 for PA-GFP-Tubulin/RhoGEF2-OE and PA-GFP-Tubulin/control).

745

746 **Figure 6: PA-GFP-Tubulin spreads to a greater extent in *eb1* mutant embryos**

747 A. *eb1* RNAi expressing embryos show perturbed tubulin architecture: Surface and
748 sagittal views of fixed control or *eb1* RNAi embryos, stained with Tubulin (Red),
749 Scribbled (Green) and DNA (Grey), show perturbed spindles in metaphase (100%, n=25
750 embryos). Scale bar=10 μ m.

751 B-E. Images from syncytial cycles of an *eb1* RNAi expressing embryo co-expressing
752 PA-GFP (B) or PA-GFP-Tubulin (D) with photoactivation at the anterior pole.

753 Kymograph for PA-GFP (B) and PA-GFP-Tubulin (E) shows increase in cortical
754 fluorescence across time while sometimes changing the extent to which the
755 fluorescence is confined. Scale bar=50 μ m, 60s.

756 F-G. Quantification of evolution of photoactivated signal across nuclear cycles in *eb1*
757 RNAi embryos. Graph depicts intensity change in PA-GFP (F) and PA-GFP-Tubulin (G)
758 for one embryo. Similar profiles were observed in multiple embryos (n=3 for each).

759 H-I. Quantification of the extent of photoactivated probe spread in XY vs XZ direction for
760 PA-GFP (H) and PA-GFP-Tubulin (I) in *eb1* RNAi embryos. The raw data is shown in a
761 lighter color and the averaged data is shown in a darker color, error bars represent
762 standard error on means (n=3 embryos for PA-GFP and PA-GFP-Tubulin each).

763 J-K. Quantification of intensity profile of photoactivated probe as measured at the end of
764 the experiment for PA-GFP (J) and PA-GFP-Tubulin (K) in *eb1* RNAi embryos. The raw
765 data is shown in a lighter color and the averaged data is shown in a darker color, error
766 bars represent standard error on means (n=3 embryos for PA-GFP-Tubulin and PA-
767 GFP each). The graph for photoactivation of PA-GFP and PA-GFP-Tubulin in control
768 embryos is the same as that shown in Figure 3I and is repeated here for comparison.

769 L. Scatter plot of length scales extracted after fitting an exponential decay function to
770 the intensity profiles seen in J and K. The values of length scales for PA-GFP and PA-
771 GFP-Tubulin for anterior photoactivation in control embryos are repeated from Figure
772 3J. (n=6,3 embryos for PA-GFP in *eb1* RNAi, 6,3 for PA-GFP-Tubulin in *eb1* RNAi. Two

773 tailed Mann-Whitney non-parametric test, p value 0.81 for PA-GFP and PA-GFP-
774 Tubulin in *eb1* RNAi, 0.02 for PA-GFP/*eb1* RNAi and PA-GFP/control, 0.04 for PA-GFP-
775 Tubulin/*eb1* RNAi and PA-GFP-Tubulin/control).

776

777 **Figure 7: Model for regulation of gradient formation across the nucleo-**
778 **cytoplasmic domains in the syncytial *Drosophila* embryo**

779 Photoactivated PA-GFP-Tubulin and PA-GFP form a cortical gradient in the syncytial
780 blastoderm embryo. RhoGEF2 overexpression causes loss of plasma membrane
781 furrows and increased spread of the anteriorly induced PA-GFP-Tubulin gradient. EB1
782 loss causes perturbation of the microtubule cytoskeleton and increased spread of the
783 anteriorly induced PA-GFP-Tubulin gradient.

784

785 **Supplementary Movies**

786

787 S1: Cytoplasmic GFP: GFP expressed under the *ubi* promoter is imaged across the
788 syncytial division cycles. Note that GFP enters the nuclei in interphase.

789 S2: mCherry-Tubulin: mCherry-Tubulin expressed with *mat*-Gal4 is imaged in the
790 syncytial division cycles. Note mCherry-Tubulin incorporation into centrosome, spindle
791 and cortical microtubules.

792 S3: PA-GFP anterior photoactivation: Region of interest at the anterior is photoactivated
793 to create a source of PA-GFP. Note that PA-GFP enters the nuclei in interphase.

794 S4: PA-GFP-Tubulin anterior photoactivation: Region of interest at the anterior is
795 photoactivated to create a source of PA-GFP-Tubulin. Note PA-GFP-Tubulin
796 incorporation into centrosome, spindle and cortical microtubules.

797 S5: PA-GFP middle photoactivation: Region of interest in the middle of the embryo is
798 photoactivated to create a source of PA-GFP.

799 S6: PA-GFP-Tubulin middle photoactivation: Region of interest in the middle of the
800 embryo is photoactivated to create a source of PA-GFP-Tubulin.

801 S7: PA-GFP anterior photoactivation in RhoGEF2-OE embryos: Region of interest at
802 the anterior is photoactivated to create a source of PA-GFP in RhoGEF2-OE embryos.

803 S8: PA-GFP-Tubulin anterior photoactivation in RhoGEF2 mutants: Region of interest at
804 the anterior is photoactivated to create a source of PA-GFP-Tubulin in RhoGEF2-OE
805 embryos.

806 S9: PA-GFP anterior photoactivation in *eb1* mutant embryos: Region of interest at the
807 anterior is photoactivated to create a source of PA-GFP in *eb1* RNAi expressing
808 embryos

809 S10: PA-GFP-Tubulin anterior photoactivation in EB1 mutants: Region of interest at the
810 anterior is photoactivated to create a source of PA-GFP-Tubulin in *eb1* RNAi expressing
811 embryos. Note the undulations caused by yolk contractions and that the cytoplasm
812 remains peripheral, without mixing with the embryo yolk region.

813 All movies are in shown in 16 color intensity rainbow scale where Blue represents the
814 lowest intensity and red represents the highest intensity. Scale bar=10 μ m or 50 μ m as
815 mentioned.

816

817

818 **References**

819 ANDERSON CA, ESER U, KORNDORF T, BORSUK ME, SKOTHEIM JM, GLADFELTER AS
820 (2013). Nuclear Repulsion Enables Division Autonomy in a Single Cytoplasm. *CurrBiol* 23:
821 1999–2010.

822 BALASUBRAMANIAN R, ZHANG X (2016). Mechanisms of FGF gradient formation during
823 embryogenesis. *Semin Cell Dev Biol* 53: 94–100.

824 BARMCHI MP, ROGERS S, HÄCKER U (2005). DRhoGEF2 regulates actin organization and
825 contractility in the Drosophila blastoderm embryo. *J Cell Biol* 168: 575–585.

826 BEREZHKOVSII AM, SAMPLE C, SHVARTSMAN SY (2010). How long does it take to
827 establish a morphogen gradient? *Biophys J* 99: L59–61.

828 BLANKENSHIP JT, WIESCHAUS E (2001). Two new roles for the Drosophila AP patterning
829 system in early morphogenesis. *Development* 128: 5129–5138.

830 CAI X, AKBER M, SPIROV A, BAUMGARTNER S (2017). Cortical movement of Bicoid in early
831 Drosophila embryos is actin- and microtubule-dependent and disagrees with the SDD
832 diffusion model. *PLoS One* 12: e0185443.

833 CAO J, ALBERTSON R, RIGGS B, FIELD CM, SULLIVAN W (2008). Nuf, a Rab11 effector,
834 maintains cytokinetic furrow integrity by promoting local actin polymerization. *J Cell Biol*
835 182: 301–313.

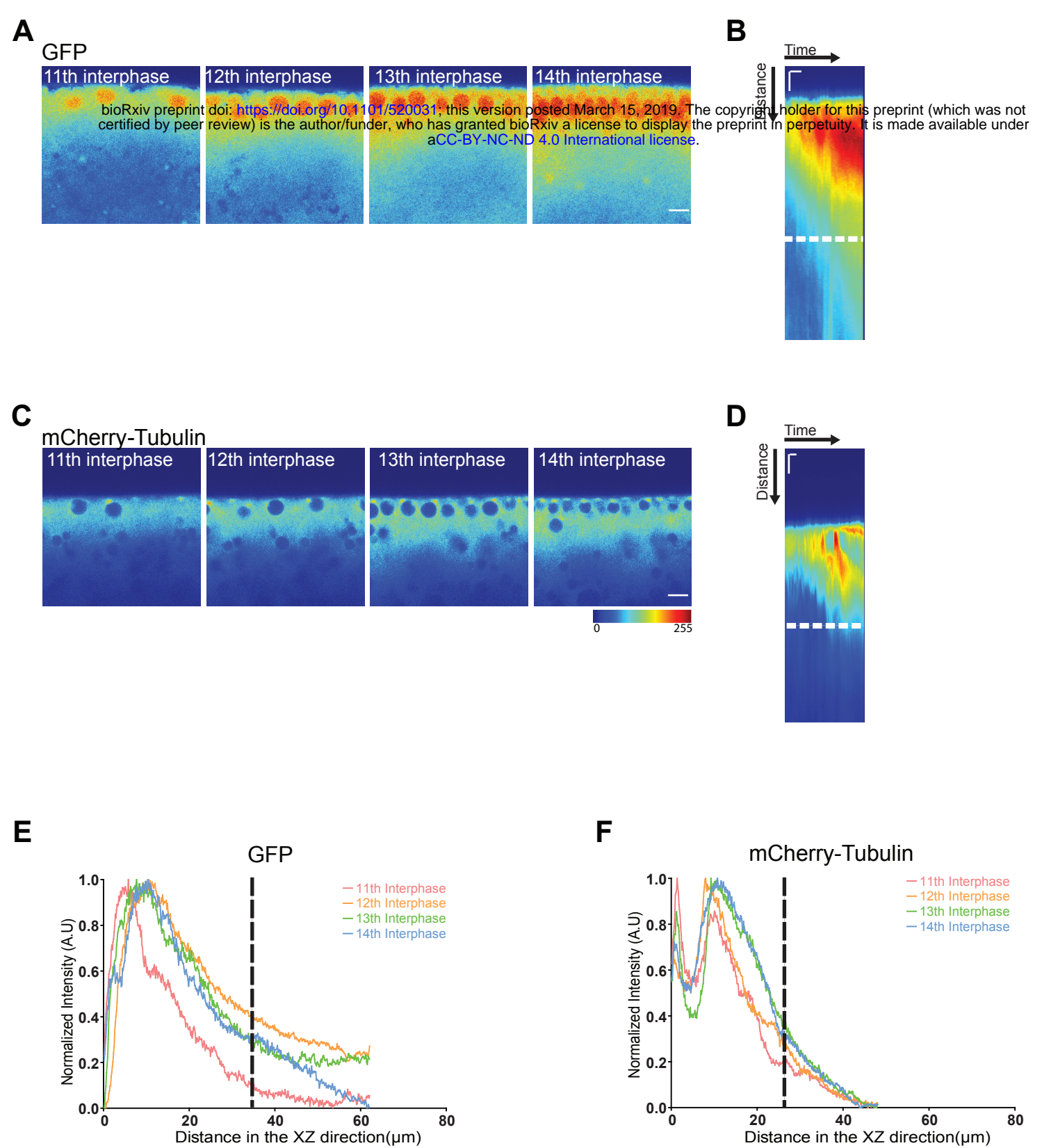
836 CAO J, CREST J, FASULO B, SULLIVAN W (2010). Cortical actin dynamics facilitate early-

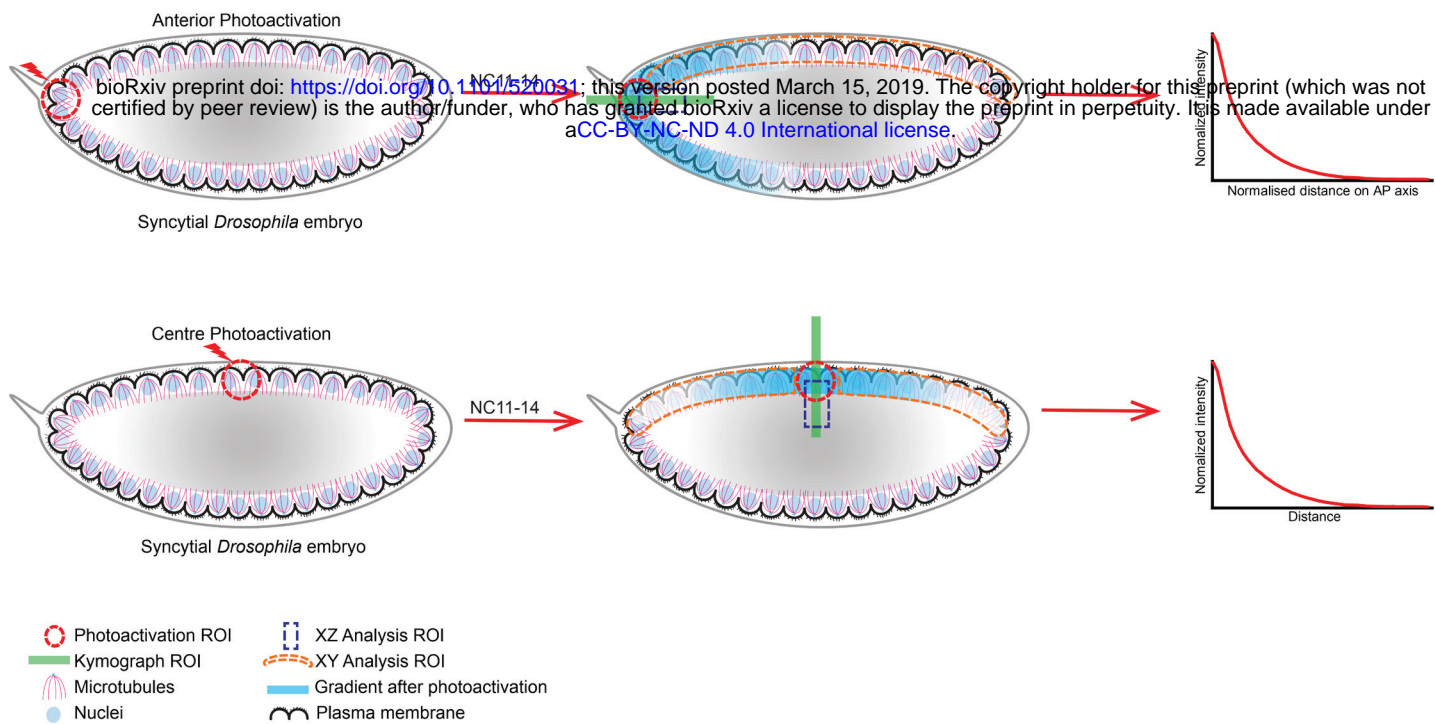
- 837 stage centrosome separation. *CurrBiol* 20: 770–776.
- 838 CARRELL SN, O'CONNELL MD, JACOBSEN T, ALLEN AE, SMITH SM, REEVES GT (2017).
839 A facilitated diffusion mechanism establishes the Drosophila Dorsal gradient. *Development*:
840 dev.155549.
- 841 CHEN J, LIPPINCOTT-SCHWARTZ J, LIU J (2012). Intracellular spatial localization regulated
842 by the microtubule network. *PLoS One* 7: e34919.
- 843 CHOWDHARY S, TOMER D, DUBAL D, SAMBRE D, RIKHY R (2017). Analysis of
844 mitochondrial organization and function in the Drosophila blastoderm embryo. *Sci Rep* 7:
845 5502.
- 846 CREST J, CONCHA-MOORE K, SULLIVAN W (2012). RhoGEF and Positioning of Rappaport-
847 like Furrows in the Early Drosophila Embryo. *CurrBiol* 22: 2037–2041.
- 848 CRICK F (1970). Diffusion in Embryogenesis. *Nature* 225: 420–422.
- 849 DANIELS BR, RIKHY R, RENZ M, DOBROWSKY TM, LIPPINCOTT-SCHWARTZ J (2012).
850 Multiscale diffusion in the mitotic Drosophila melanogaster syncytial blastoderm. *Proc Natl*
851 *Acad Sci U S A* 109: 8588–8593.
- 852 DELOTTO R, DELOTTO Y, STEWARD R, LIPPINCOTT-SCHWARTZ J (2007).
853 Nucleocytoplasmic shuttling mediates the dynamic maintenance of nuclear Dorsal levels
854 during Drosophila embryogenesis. *Development* 134: 4233–4241.
- 855 DUNDON SER, CHANG S-S, KUMAR A, OCCHIPINTI P, SHROFF H, ROPER M,
856 GLADFELTER AS (2016). Clustered nuclei maintain autonomy and nucleocytoplasmic ratio
857 control in a syncytium. *MolBiol Cell* 27: 2000–2007.
- 858 DURRIEU L, KIRRMAYER D, SCHNEIDT T, KATS I, RAGHAVAN S, HUFNAGEL L,
859 SAUNDERS TE, KNOP M (2018). Bicoid gradient formation mechanism and dynamics
860 revealed by protein lifetime analysis. *MolSystBiol* 14: e8355.
- 861 FAHMY K, AKBER M, CAI X, KOUL A, HAYDER A, BAUMGARTNER S (2014). α Tubulin 67C
862 and Ncd are essential for establishing a cortical microtubular network and formation of the
863 Bicoid mRNA gradient in Drosophila. *PLoS One* 9: e112053.
- 864 FIGARD L, XU H, GARCIA HG, GOLDING I, SOKAC AM (2013). The plasma membrane
865 flattens out to fuel cell-surface growth during Drosophila cellularization. *Dev Cell* 27: 648–
866 655.
- 867 FOE, ODELL AND EDGAR (1993). Mitosis and morphogenesis in the Drosophila embryo: point
868 and counterpoint. In *The Development of Drosophila melanogaster* (Ed. AMA Michael
869 Bates). Cold Spring Harbor Laboratory Press., pp. 149–300.
- 870 FOE VE, ALBERTS BM (1983). Studies of nuclear and cytoplasmic behaviour during the five
871 mitotic cycles that precede gastrulation in Drosophila embryogenesis. *J Cell Sci* 61: 31–70.
- 872 FRESCAS D, MAVRAKIS M, LORENZ H, DELOTTO R, LIPPINCOTT-SCHWARTZ J (2006).
873 The secretory membrane system in the Drosophila syncytial blastoderm embryo exists as
874 functionally compartmentalized units around individual nuclei. *J Cell Biol* 173: 219–230.

- 875 GAUTHIER-KEMPER A, WEISSMANN C, REYHER H-J, BRANDT R (2012). Monitoring
876 cytoskeletal dynamics in living neurons using fluorescence photoactivation. *Methods*
877 *Enzymol* 505: 3–21.
- 878 GOODSSELL DS (2013). *The Machinery of Life*. Springer Science & Business Media.
- 879 GREGOR T, BIALEK W, DE RUYTER VAN STEVENINCK RR, TANK DW, WIESCHAUS EF
880 (2005). Diffusion and scaling during early embryonic pattern formation. *Proc Natl Acad Sci*
881 *U S A* 102: 18403–18407.
- 882 GREGOR T, WIESCHAUS EF, MCGREGOR AP, BIALEK W, TANK DW (2007). Stability and
883 nuclear dynamics of the bicoid morphogen gradient. *Cell* 130: 141–152.
- 884 GRIMM O, COPPEY M, WIESCHAUS E (2010). Modelling the Bicoid gradient. *Development*
885 137: 2253–2264.
- 886 GURA SADOVSKY R, BRIELLE S, KAGANOVICH D, ENGLAND JL (2017). Measurement of
887 Rapid Protein Diffusion in the Cytoplasm by Photo-Converted Intensity Profile Expansion.
888 *Cell Rep* 18: 2795–2806.
- 889 KARR TL (1986). Organization of the cytoskeleton in early *Drosophila* embryos. *J Cell Biol* 102:
890 1494–1509.
- 891 KELLOGG DR, MITCHISON TJ, ALBERTS BM (1988). Behaviour of microtubules and actin
892 filaments in living *Drosophila* embryos. *Development* 103: 675–686.
- 893 KUHN H, SOPKO R, COUGHLIN M, PERRIMON N, MITCHISON T (2015). The Atg1-Tor
894 pathway regulates yolk catabolism in *Drosophila* embryos. *Development* 142: 3869–3878.
- 895 LEE C, ZHANG H, BAKER AE, OCCHIPINTI P, BORSUK ME, GLADFELTER AS (2013).
896 Protein aggregation behavior regulates cyclin transcript localization and cell-cycle control.
897 *Dev Cell* 25: 572–584.
- 898 LITTLE SC, TKAČIK G, KNEELAND TB, WIESCHAUS EF, GREGOR T (2011). The formation
899 of the Bicoid morphogen gradient requires protein movement from anteriorly localized
900 mRNA. *PLoS Biol* 9: e1000596.
- 901 LUBY-PHELPS K (2000). Cytoarchitecture and physical properties of cytoplasm: volume,
902 viscosity, diffusion, intracellular surface area. *Int Rev Cytol* 192: 189–221.
- 903 MAVRAKIS M, RIKHY R, LIPPINCOTT-SCHWARTZ J (2009a). Cells within a cell: Insights into
904 cellular architecture and polarization from the organization of the early fly embryo.
905 *CommunIntegrBiol* 2: 313–314.
- 906 MAVRAKIS M, RIKHY R, LIPPINCOTT-SCHWARTZ J (2009b). Plasma membrane polarity and
907 compartmentalization are established before cellularization in the fly embryo. *Dev Cell* 16:
908 93–104.
- 909 PARRY BR, SUROVTSEV IV, CABEEN MT, O'HERN CS, DUFRESNE ER, JACOBS-
910 WAGNER C (2014). The bacterial cytoplasm has glass-like properties and is fluidized by
911 metabolic activity. *Cell* 156: 183–194.
- 912 PAVLATH GK, RICH K, WEBSTER SG, BLAU HM (1989). Localization of muscle gene

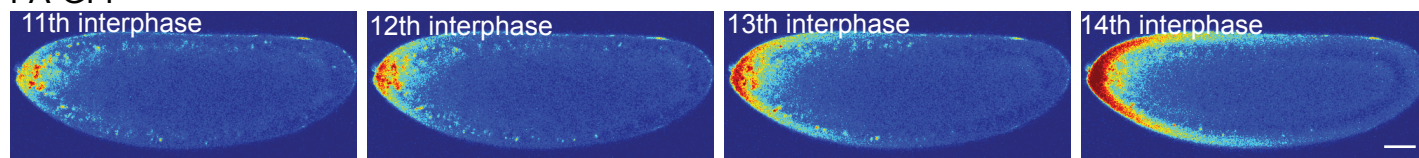
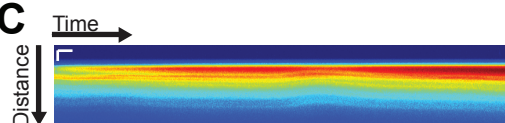
- 913 products in nuclear domains. *Nature* 337: 570–573.
- 914 ROGERS SL, ROGERS GC, SHARP DJ, VALE RD (2002). *Drosophila* EB1 is important for
915 proper assembly, dynamics, and positioning of the mitotic spindle. *J Cell Biol* 158: 873–884.
- 916 RUIWEN WANG MGB (2007). The maximal size of protein to diffuse through the nuclear pore is
917 larger than 60kDa. *FEBS Lett* 581: 3164.
- 918 RUPPRECHT J-F, ONG KH, YIN J, HUANG A, DINH H-H-Q, SINGH AP, ZHANG S, YU W,
919 SAUNDERS TE (2017). Geometric constraints alter cell arrangements within curved
920 epithelial tissues. *MolBiol Cell* 28: 3582–3594.
- 921 RUSAN NM, PEIFER M (2007). A role for a novel centrosome cycle in asymmetric cell division.
922 *J Cell Biol* 177: 13–20.
- 923 SCHMIDT A, GROSSHANS J (2018). Dynamics of cortical domains in early development. *J Cell*
924 *Sci* 131.
- 925 SHERLEKAR A, RIKHY R (2016). Syndapin promotes pseudocleavage furrow formation by
926 actin organization in the syncytial *Drosophila* embryo. *MolBiol Cell* 27: 2064–2079.
- 927 SHVARTSMAN SY, COPPEY M, BEREZHKOVSII AM (2008). Dynamics of maternal
928 morphogen gradients in *Drosophila*. *CurrOpin Genet Dev* 18: 342–347.
- 929 SPIROV A, FAHMY K, SCHNEIDER M, FREI E, NOLL M, BAUMGARTNER S (2009).
930 Formation of the bicoid morphogen gradient: an mRNA gradient dictates the protein
931 gradient. *Development* 136: 605–614.
- 932 SULLIVAN W, THEURKAUF WE (1995). The cytoskeleton and morphogenesis of the early
933 *Drosophila* embryo. *CurrOpin Cell Biol* 7: 18–22.
- 934 TURNER FR, MAHOWALD AP (1976). Scanning electron microscopy of *Drosophila*
935 embryogenesis: 1. The structure of the egg envelopes and the formation of the cellular
936 blastoderm. *Dev Biol* 50: 95–108.
- 937 VERKMAN AS (1999). [22] Green fluorescent protein as a probe to study intracellular solute
938 diffusion. In *Methods in Enzymology* Academic Press, pp. 250–264.
- 939 WARN RM (1986). The cytoskeleton of the early *Drosophila* embryo. *J Cell Sci Suppl* 5: 311–
940 328.
- 941 WELTE MA (2015). As the fat flies: The dynamic lipid droplets of *Drosophila* embryos.
942 *BiochimBiophys Acta* 1851: 1156–1185.
- 943 WESSEL AD, GUMALLA M, GROSSHANS J, SCHMIDT CF (2015). The mechanical properties
944 of early *Drosophila* embryos measured by high-speed video microrheology. *Biophys J* 108:
945 1899–1907.
- 946 ZHANG Y, YU JC, JIANG T, FERNANDEZ-GONZALEZ R, HARRIS TJC (2018). Collision of
947 Expanding Actin Caps with Actomyosin Borders for Cortical Bending and Mitotic Rounding
948 in a Syncytium. *Dev Cell* 45: 551–564.e4.

949

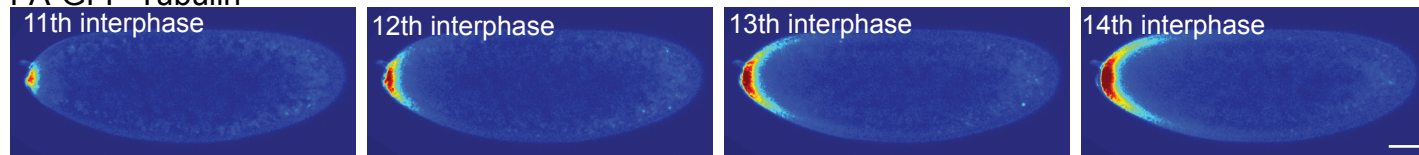
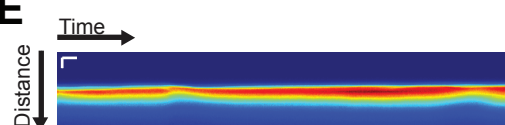
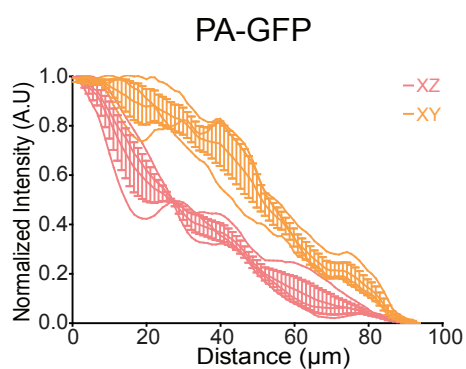
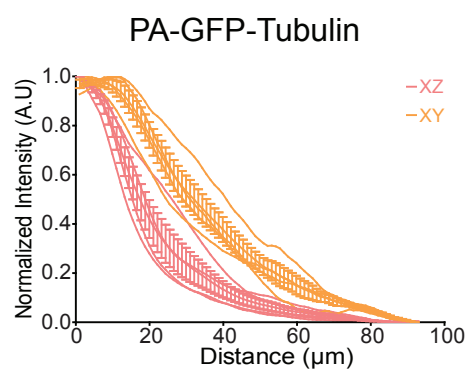


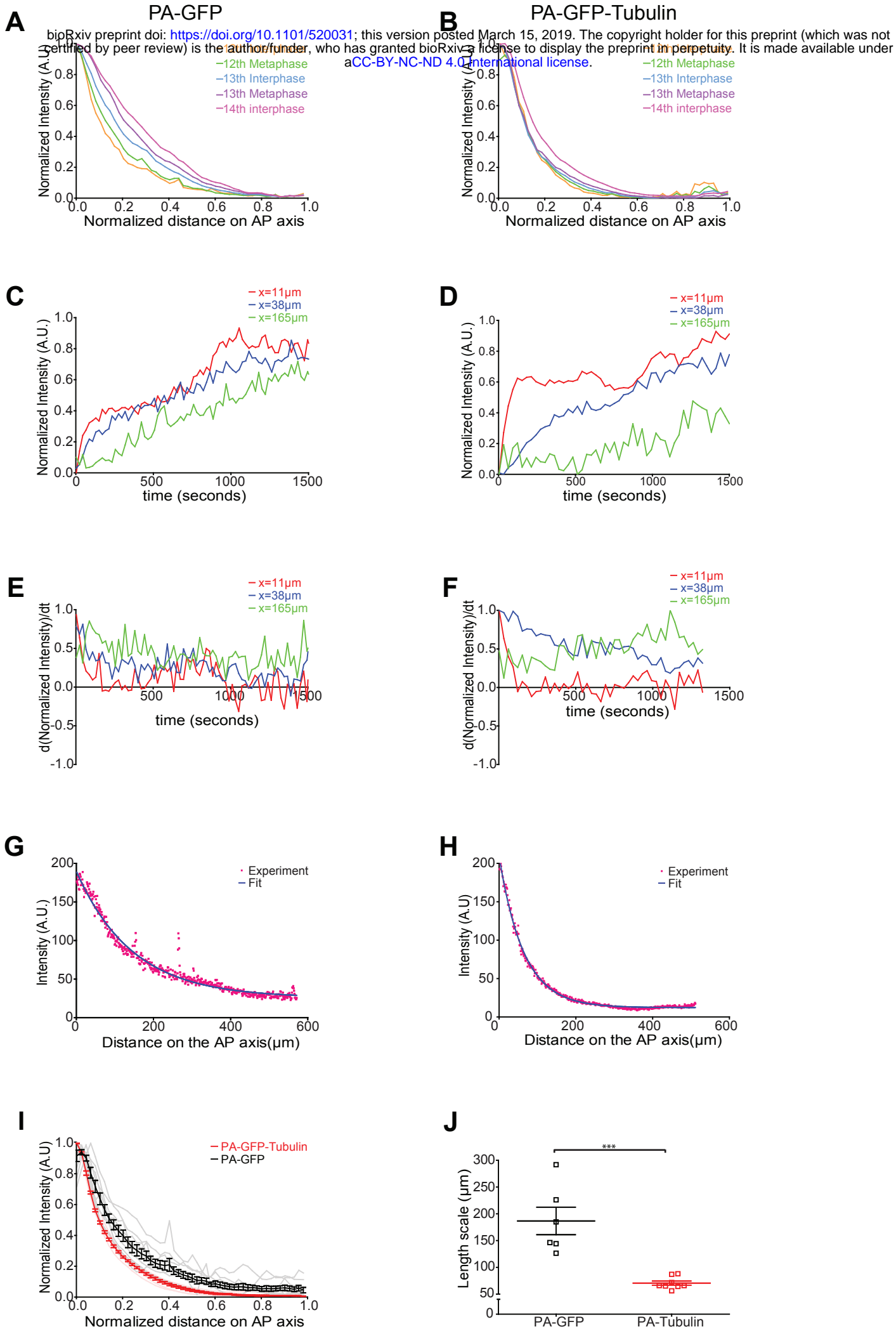
A**B**

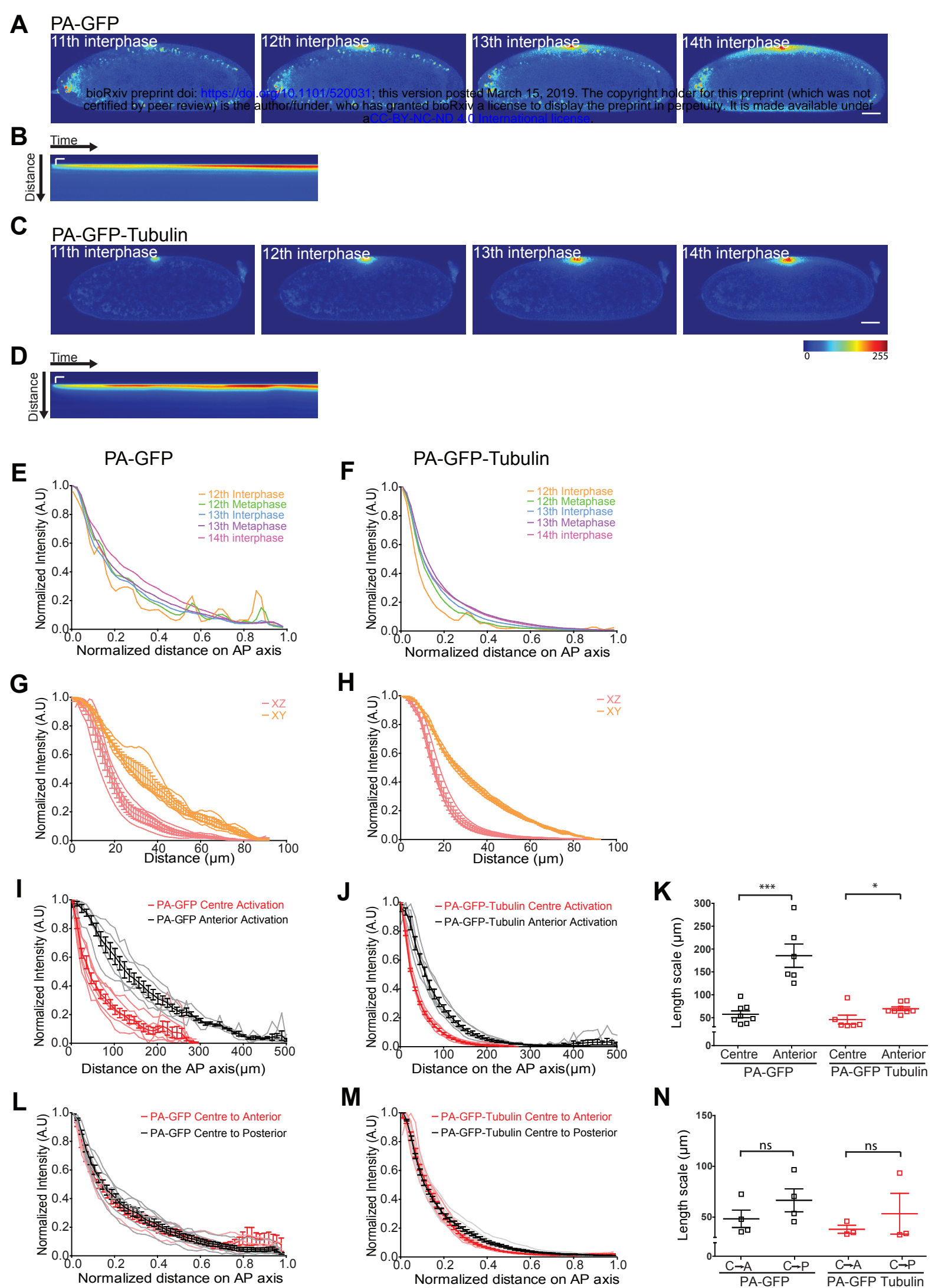
PA-GFP

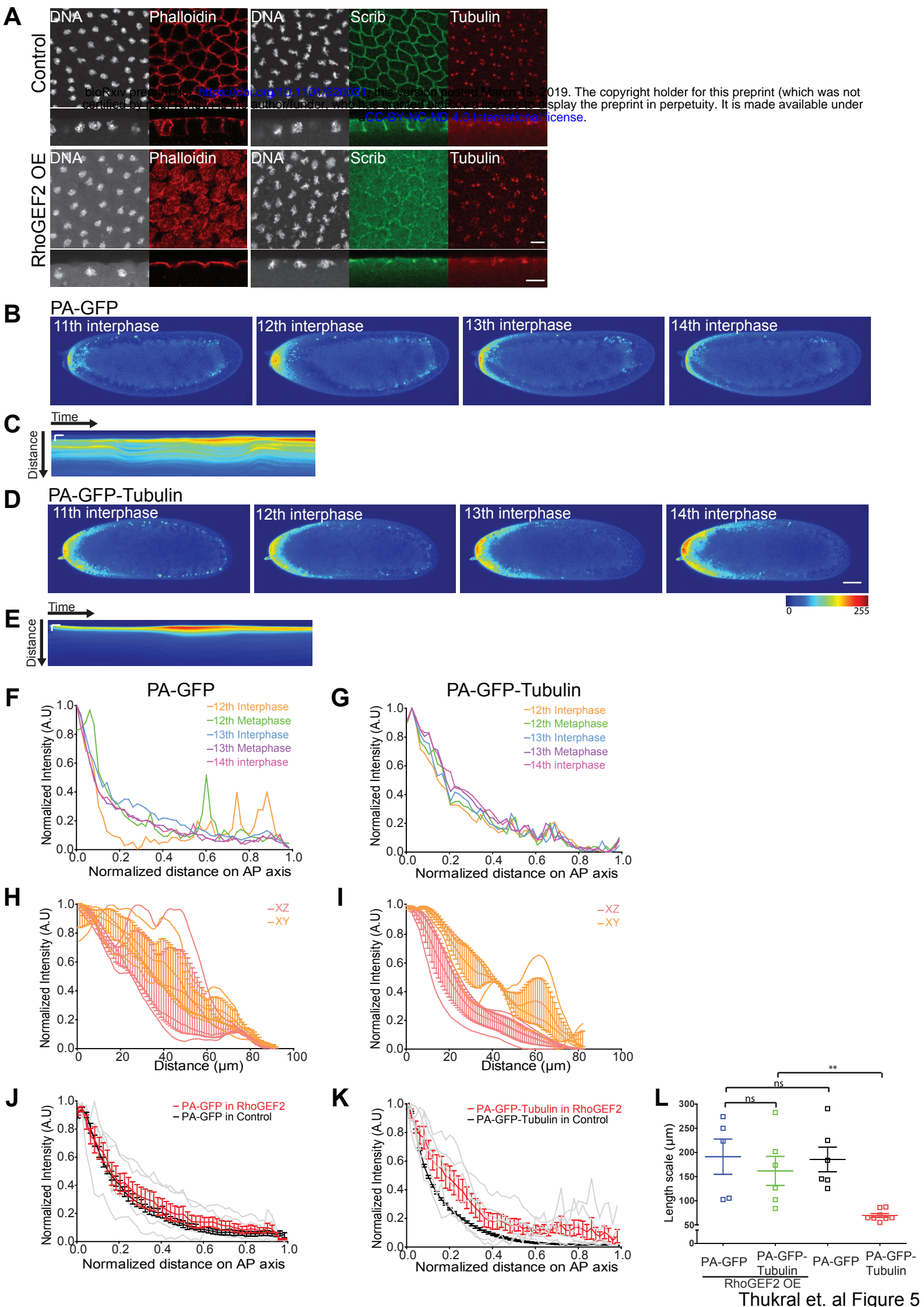
**C****D**

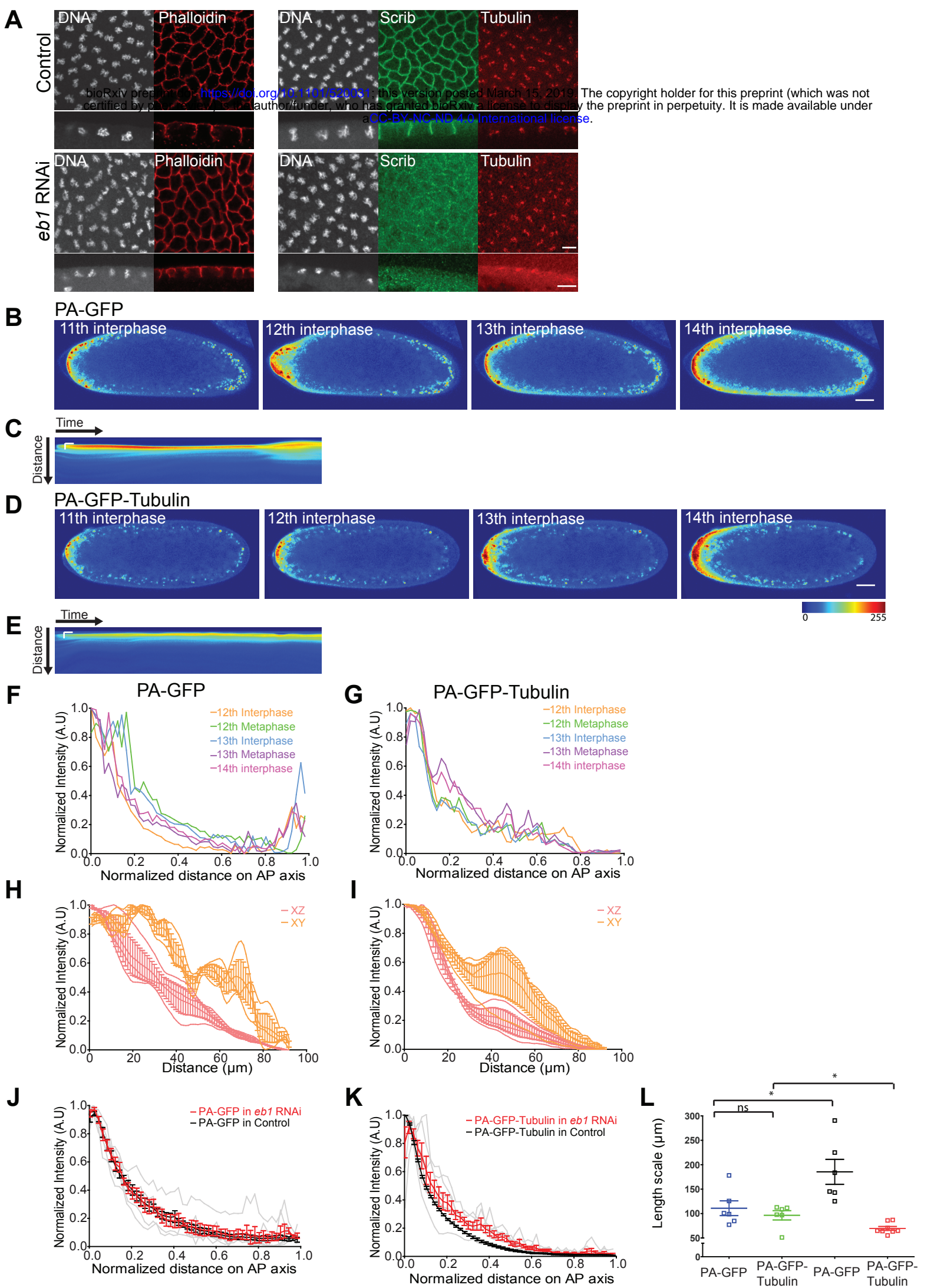
PA-GFP-Tubulin

**E****F****G**









Syncytial *Drosophila* embryo

